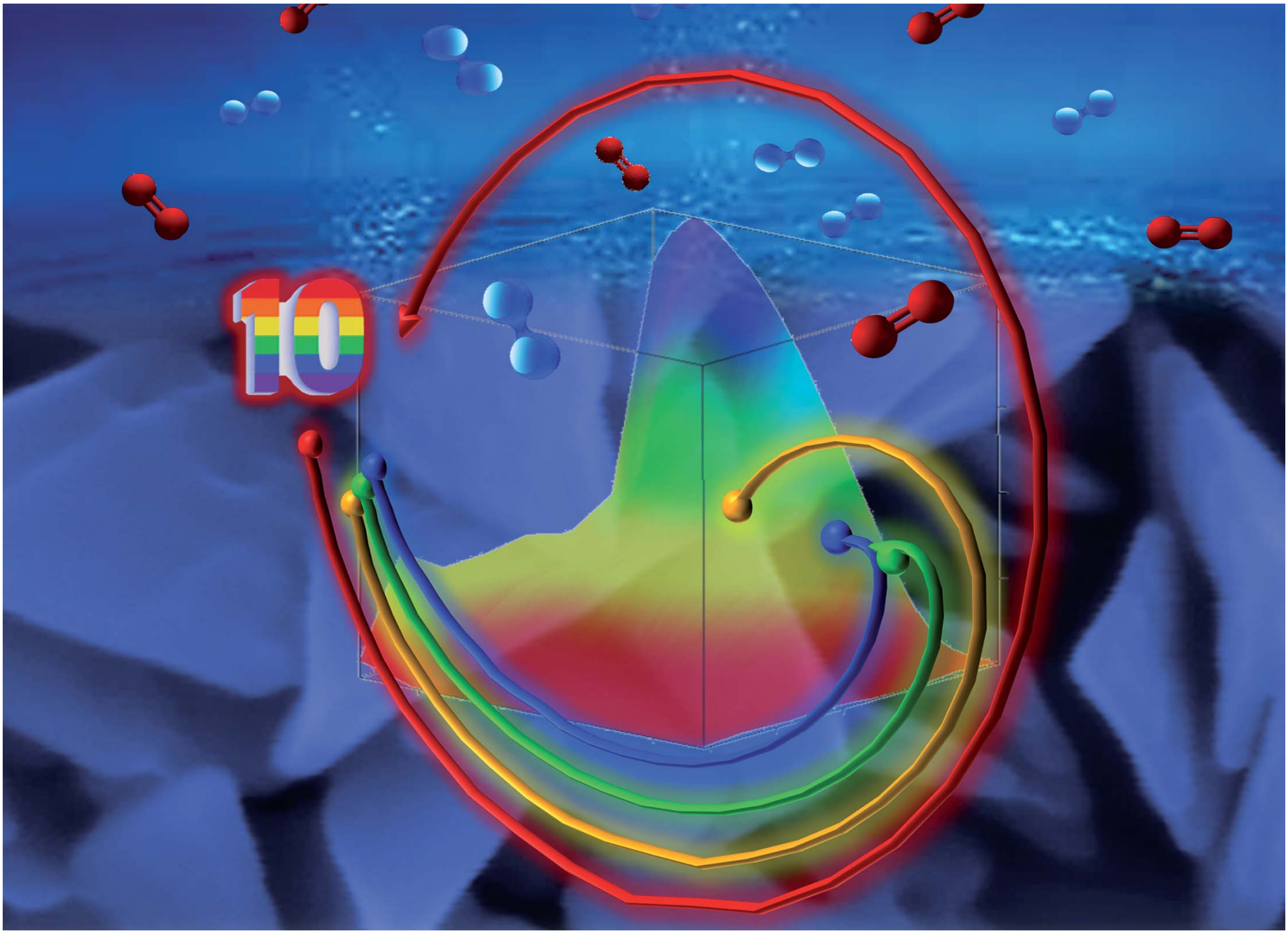

**Showcasing research from Padova University, CNR-ICMATE, and INSTM, Padova, Italy, in collaboration with Laboratoire CRISMAT, CNRS, Caen, France, GFZ German Research Centre, Potsdam, and Ruhr University Bochum, Germany.**

Advances in photo-assisted seawater splitting promoted by green iron oxide-carbon nitride photoelectrocatalysts

$Fe_2O_3$/graphitic carbon nitride (gCN) photoelectrocatalysts for seawater splitting are developed by a hybrid plasma-assisted vapor phase/electrophoretic deposition. The best performances correspond to a Tafel slope of ≈100 mV dec$^{-1}$ and an overpotential <350 mV, enabling exclusion of the competitive hypochlorite formation. This behavior, accompanied by the remarkable durability, opens the door to a profitable exploitation of natural resources for clean energy production with no environmental footprint.

## As featured in:

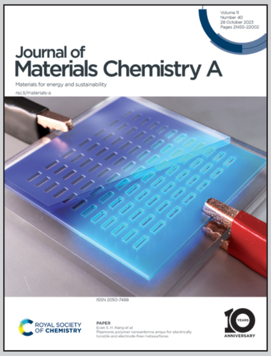

See Gian Andrea Rizzi, Chiara Maccato *et al.*, *J. Mater. Chem. A*, 2023, **11**, 21595.

ROYAL SOCIETY
OF **CHEMISTRY**

rsc.li/materials-a

Registered charity number: 207890

Journal of
Materials Chemistry A

ROYAL SOCIETY
OF CHEMISTRY

PAPER

View Article Online
View Journal | View Issue

Check for updates

Cite this: *J. Mater. Chem. A*, 2023, **11**, 21595

# Advances in photo-assisted seawater splitting promoted by green iron oxide-carbon nitride photoelectrocatalysts†

Mattia Benedet,[ab] Gian Andrea Rizzi,*[ab] Oleg I. Lebedev,[c] Vladimir Roddatis,[d] Cinzia Sada,[e] Jan-Lucas Wree,[f] Anjana Devi,[f] Chiara Maccato,*[ab] Alberto Gasparotto[ab] and Davide Barreca[b]

Received 24th July 2023
Accepted 14th September 2023

DOI: 10.1039/d3ta04363k

rsc.li/materials-a

Solar-driven seawater electrolysis for hydrogen fuel production holds an outstanding potential towards the development of a carbon-neutral and sustainable energy infrastructure, but the development of green, efficient and stable photoelectrocatalysts selectively promoting oxygen evolution remains a formidable challenge. Motivated by this issue, in this work we propose a tailored combination of two economically viable materials, $\alpha$-$Fe_2O_3$ and graphitic carbon nitride (gCN), to fabricate promising anodes – eventually decorated with cobalt phosphate (CoPi) particles – for alkaline seawater photosplitting. The target systems were fabricated *via* an original multi-step route, involving the plasma-enhanced chemical vapor deposition of iron(III) oxide on conducting glasses, the introduction of gCN in very small amounts by a rapid and facile electrophoretic process, and final annealing in air. A comprehensive characterization revealed the successful fabrication of composites featuring a tailored surface defectivity, a controlled nano-organization, and a close $Fe_2O_3$/gCN interfacial contact. After decoration with CoPi, the best performances corresponded to a Tafel slope of ≈100 mV dec$^{-1}$ and overpotential values enabling us to rule out the competitive hypochlorite formation. In addition, photocurrent densities at 1.23 V *vs.* RHE showed a nearly 7-fold increase upon $Fe_2O_3$ functionalization with both gCN and CoPi. These amenable results, directly dependent on the electronic interplay at $Fe_2O_3$/gCN heterojunctions and on CoPi beneficial effects, are accompanied by a remarkable long-term stability, and may open up attractive avenues for clean energy production using natural resources.

## 1. Introduction

Molecular hydrogen ($H_2$) is expected to play an important role in driving mankind on the road to carbon neutrality, a foremost challenge to achieve "net-zero emissions" by 2050.[1–11] Differently from $H_2$ produced from fossil fuels ('grey hydrogen'), in conflict with the achievement of these objectives, 'green hydrogen' obtained by electrochemical water splitting, possibly activated by sunlight, is environmentally friendly and renewable, and has gained remarkable interest to solve the global energy crisis and shape a sustainable energy economy.[1,12–19] Nonetheless, the water splitting efficiency is limited by the kinetic barrier of the anodic oxygen evolution reaction (OER), possessing a high overpotential ($\eta$).[9,14,17,20–23] The current benchmark OER electrocatalysts based on noble-metal (*e.g.*, Ir and Ru) oxides suffer from scarcity, high cost and modest long-term stability, limiting their large-scale use and commercialization.[1,12,14,24,25] Therefore, significant efforts have been devoted to the development of non-precious metal (photo)electrocatalysts including oxides, hydroxides, and nitrides.[5,6,8,14,26,27]

In view of real-world exploitation, one of the less discussed, though important, requirements is the availability of water feedstocks. Although freshwater is readily available on a laboratory scale, the need for significant freshwater feeds for practical applications may become a bottleneck especially in hot/arid coastal regions, which, however, have immediate access to seawater.[1,9,11,28] In fact, the use of the latter, an almost endless natural resource, representing ≈97% of the total Earth water reservoirs, could substantially help to alleviate freshwater shortage.[1,24,28–32] In this regard, coupling seawater electrolysis with renewable energy sources,[1,28,33] such as solar light,[2,8,15,34,35] opens up attractive avenues for the large-scale generation and

---

[a] *Department of Chemical Sciences, Padova University and INSTM, 35131 Padova, Italy*

[b] *CNR-ICMATE and INSTM, Department of Chemical Sciences, Padova University, 35131 Padova, Italy. E-mail: gianandrea.rizzi@unipd.it; chiara.maccato@unipd.it*

[c] *Laboratoire CRISMAT, UMR 6508 Normandie Université, CNRS, ENSICAEN, UNICAEN, 14050 Caen, Cedex 4, France*

[d] *GFZ German Research Centre for Geosciences, 14473, Potsdam, Germany*

[e] *Department of Physics and Astronomy, Padova University and INSTM, 35131 Padova, Italy*

[f] *Inorganic Materials Chemistry, Ruhr University Bochum, 44801 Bochum, Germany*

† Electronic supplementary information (ESI) available. See DOI: https://doi.org/10.1039/d3ta04363k

conversion of sustainable energy through natural capital exploitation.[36]

Although much progress has been achieved so far in designing efficient OER seawater (photo)electrocatalysts in various ways,[1,10,11,20,30,37] there are still various open issues to be properly tackled for seawater deployment in real-world environments:[38] (i) optimization of catalyst's long-term stability,[30] as required for industrial applications, possibly coupled to the utilization of low cost, largely abundant and eco-friendly materials and (ii) manufacturing of anodes selective towards OER against the competitive hypochlorite formation ($Cl^- + 2OH^- \rightarrow ClO^- + H_2O + 2e^-$), the latter being thermodynamically more demanding, but kinetically favoured.[1,10,22,28,39,40] In this regard, it is worth highlighting that, if OER is carried out in alkaline solutions at an overpotential <0.48 V, $ClO^-$ generation from chloride oxidation can be favourably suppressed.[1,20,39,41]

In the broad scenario of OER photoelectrocatalysts, *hematite* ($\alpha$-$Fe_2O_3$), the most stable iron(III) oxide polymorph,[4,15,16,23,42] is one of the most promising platforms due to its natural abundance, biocompatibility, low cost, good stability, and band gap ($E_G \approx 2.1$ eV) enabling the absorption of a large solar spectrum portion.[2,6,12,16,23,43,44] These advantages are partially eclipsed by its small exciton diffusion length (≈2–4 nm), as well as by the poor mobility and low lifetime of photogenerated charge carriers (<10 ps), restricting its practical applications.[6,7,13,16,43,45,46] Among the strategies proposed to overcome these shortfalls,[23,47,48] a valuable alternative is offered by the construction of heterojunctions with staggered band alignment, yielding improved sunlight harvesting and more efficient electron–hole separation.[13–17,36,42,49]

In this regard, a very attractive candidate to be combined with $Fe_2O_3$ is graphitic carbon nitride (gCN), a research hotspot in recent years.[3,15,17,18,42,43,48,50] gCN, a 2D metal-free material endowed with high chemical stability, structural flexibility, tuneable defectivity and moderate band gap energy ($E_G \approx 2.4$–2.8 eV),[5,19,34,35,49,51–55] has been widely explored as a Vis-light-active photocatalyst.[45,46,49,56–58] Recent studies have demonstrated that $Fe_2O_3$/gCN heterostructured systems hold a significant potential as Vis-light photo(electro)catalysts for pollutant degradation[26,42,51,54,59] and $CO_2$ reduction,[47,53] as well as for $H_2$ production by direct photocatalysis[2–4,17,18,44,49,60] and electrochemically assisted processes in freshwater.[12–14,19,34,45,50,56]

Up to date, the use of $Fe_2O_3$- and gCN-containing materials for seawater splitting has been reported in photocatalytic,[31,32,61,62] electrochemical[22,24,41] and photoelectrochemical processes.[6,21,36,37,63] Nevertheless, to the best of our knowledge, no literature works employing $Fe_2O_3$-gCN composites for such end-uses are available so far. Therefore, the interplay between the chemico-physical characteristics of similar nanomaterials and their functional behaviour requires further studies to develop stable and selective anodes for OER in seawater.

In view of the target application, an imperative issue is the implementation of a highly controllable preparation route affording a convenient modulation of material properties[20] and an effective component interfacial contact, to promote electron–hole separation, improve photostability, and boost light absorption.[3,13] Thus far, $Fe_2O_3$-gCN catalysts for various end-uses have been prepared either in a powdered form, or through powder immobilization on substrates using additives/binders.[4,12,18,19,44,47,51–53,57,60,64] In a different way, modern frontiers for research development focus on the direct growth of $Fe_2O_3$-gCN materials onto suitable substrates.[20,35,48] Related examples include: (i) $Fe_2O_3$-gCN preparation by $Fe_2O_3$ sputtering, followed by gCN drop-casting and spreading;[56] (ii) $Fe_2O_3$ electro-/solvo-/hydrothermal deposition and vapor phase/electrochemical functionalization with gCN;[42,43,45,48,49] and (iii) chemical vapor deposition (CVD) of $Fe_2O_3$ and subsequent gCN spin coating.[13]

In the present work, we report on the fabrication of stable and efficient $Fe_2O_3$-gCN photoanodes selectively promoting oxygen evolution during seawater electrolysis. The target materials were developed for the first time by a multi-step fabrication strategy (Scheme 1), involving the initial plasma-enhanced CVD (PE-CVD) of $\alpha$-$Fe_2O_3$ on fluorine-doped tin oxide (FTO)-coated glass substrates, the functionalization with tiny amounts of graphitic carbon nitride by electrophoretic deposition (EPD), and final thermal treatment in air. Both PE-CVD and EPD offer various degrees of freedom to tailor the characteristics of the resulting nanomaterials, due to the peculiar features of cold-plasmas in $Fe_2O_3$ synthesis (PE-CVD),[25,65] and the possibility of obtaining exfoliated gCN systems formed by micro/nano-sheets (EPD).[66] In fact, EPD processes were performed starting from two kinds of gCN powders with different active areas,[66–68] to investigate the interrelations between gCN characteristics and the functional performances of the obtained composites.

The adopted procedure enabled us to obtain an intimate $Fe_2O_3$/gCN interfacial contact, yielding, in turn, a reduced charge resistance, an improved OER photoactivity, and an enhanced operational stability. The developed nanocomposites were subjected to functional tests in both simulated and real seawater under alkaline conditions, analogous to those employed in the operation of industrial electrolyzers.[10,27,33] Besides material characterization by standard electrochemical techniques, we present and discuss the results obtained by intensity-modulated photocurrent spectroscopy (IMPS), which yielded accurate kinetic constants for charge recombination/transfer processes on the surface and into the solution.[69,70] To our knowledge, similar data are not available to date for $Fe_2O_3$-gCN nanocomposites. The best performing system, obtained after functionalization with cobalt(II) phosphate (CoPi), a well-known oxidation co-catalyst,[35,71] yielded an overpotential ($\eta$) < 350 mV and a Tafel slope of ≈ 100 mV $dec^{-1}$, comparing favourably with $Fe_2O_3$- or gCN-containing materials tested in seawater splitting up to date. The photocurrent density values at 1.2 V *vs.* RHE showed a nearly 7-fold increase upon $Fe_2O_3$ functionalization with both gCN and CoPi. These outcomes, accompanied by the good material selectivity and durability, offer a promising route towards the production of sustainable and green photoelectrocatalysts for the integration of renewable fuels into a grid system.

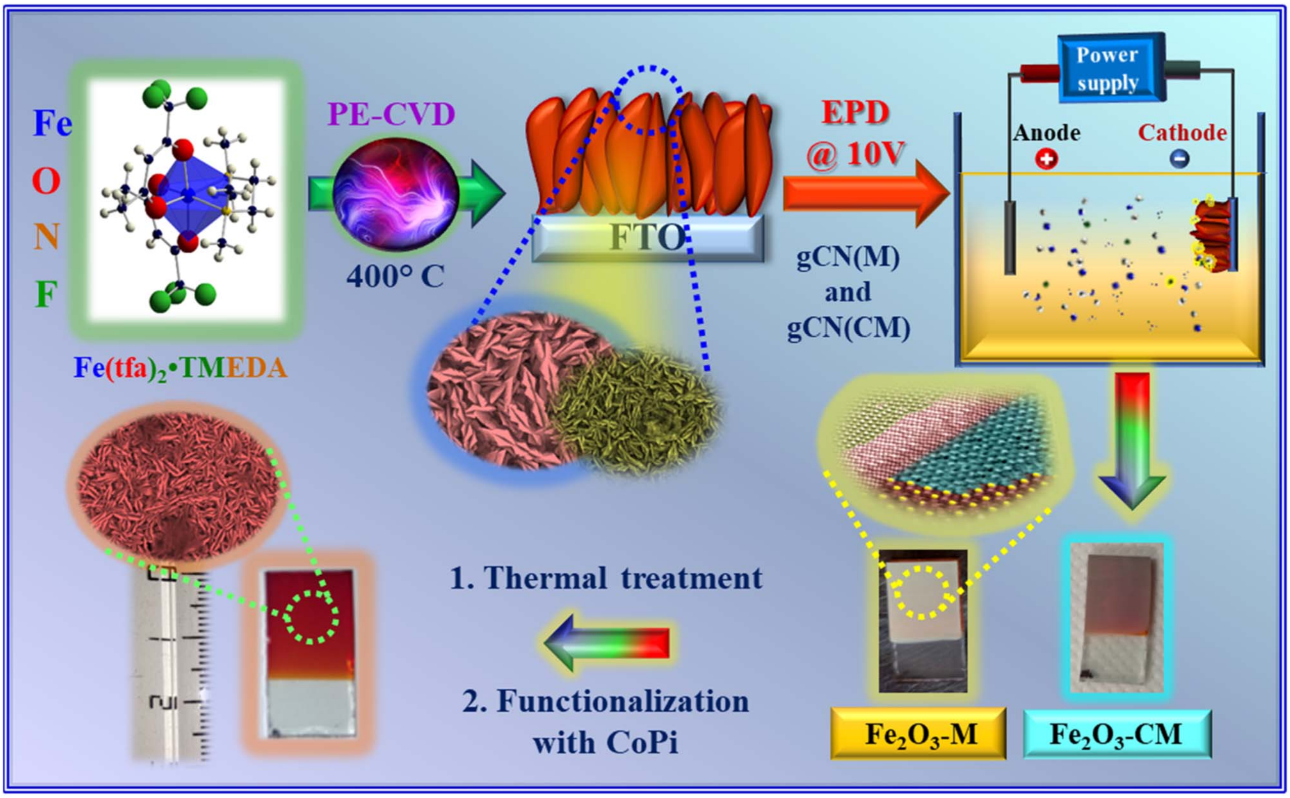

Scheme 1 Schematic illustration of the strategy used to fabricate $Fe_2O_3$ specimens functionalized with gCN.

## 2. Experimental

### 2.1 Material preparation

The adopted synthetic strategy for the preparation of $Fe_2O_3$-gCN composite materials is summarized in Scheme 1. The PE-CVD of $Fe_2O_3$ was performed on FTO glass substrates (Aldrich®; ≈7 Ω $sq^{-1}$; FTO thickness ≈600 nm) from Ar–$O_2$ plasmas at 400 °C, a temperature chosen on the basis of preliminary optimization (see ESI, Section S-2.1†).

The synthesis of two types of carbon nitride powders, namely gCN(M) and gCN(CM), obtained from melamine and from a melamine + cyanuric acid adduct, respectively, is described in the ESI (Section S-1.1.2).† Subsequently, the EPD of gCN powders on FTO-supported specimens was carried out following a previous route.[72] In a typical experiment, a suspension containing pre-grinded carbon nitride powders (40 mg), acetone (50 mL) and 10 mg of $I_2$ was sonicated for 20 min. The EPD of gCN on iron(III) oxide was performed adopting a two-electrode setup, in which the FTO-$Fe_2O_3$ sample and a carbon paper slide were used as the deposition electrode and counter-electrode, respectively. In addition, CoPi electrodeposition on selected samples was subsequently performed, with the aim to improve their OER photoelectrocatalytic activity (see ESI,† Section S-1.1.3).

In the following, specimens are labelled as $Fe_2O_3$–X–(Y), where X = M or CM, and Y = CoPi. For comparison purposes, bare $Fe_2O_3$ (with no gCN) was also prepared and analysed, either as such or after functionalization with CoPi.

### 2.2 Chemico-physical characterization

Field emission-scanning electron microscopy (FE-SEM) and energy-dispersive X-ray spectroscopy (EDXS) analyses were performed using a Zeiss SUPRA 40 VP apparatus equipped with an INCA x-act PentaFET Precision spectrometer, using primary electron beam voltages between 10 and 20 kV. The mean particle sizes were evaluated using the ImageJ® software.[73] An NT-MDT SPM Solver P47H-PRO instrument operated in tapping mode was used for atomic force microscopy (AFM) characterization. After background subtraction and plane fitting, root-mean-square roughness (RMS) values (see Fig. 1) were obtained from 2 × 2 $\mu m^2$ micrographs, as reported previously.[66] X-ray photoelectron spectroscopy (XPS) was carried out using a PHI 5000 VersaProbe instrument at a pressure $<10^{-8}$ mbar, employing a monochromatic AlKα excitation source ($h\nu = 1486.6$ eV). No preliminary sputtering was carried out. Binding energies (BEs) were corrected for charging phenomena by assigning a position of 284.8 eV to the adventitious C 1s component. Curve fitting was carried out using the XPSPEAK software, with Gaussian–Lorentzian functions.[74] Atomic percentages (at%) were calculated from peak area integration using PHI XPS V1.3.6 sensitivity factors. Secondary ion mass spectrometry (SIMS) measurements were carried out using an IMS 4f mass spectrometer (Cameca), with a $Cs^+$ primary beam (14.5 keV, 30 nA; stability = 0.2%) and an electron gun for charge compensation. Analyses were performed in beam blanking mode, rastering over a 150 × 150

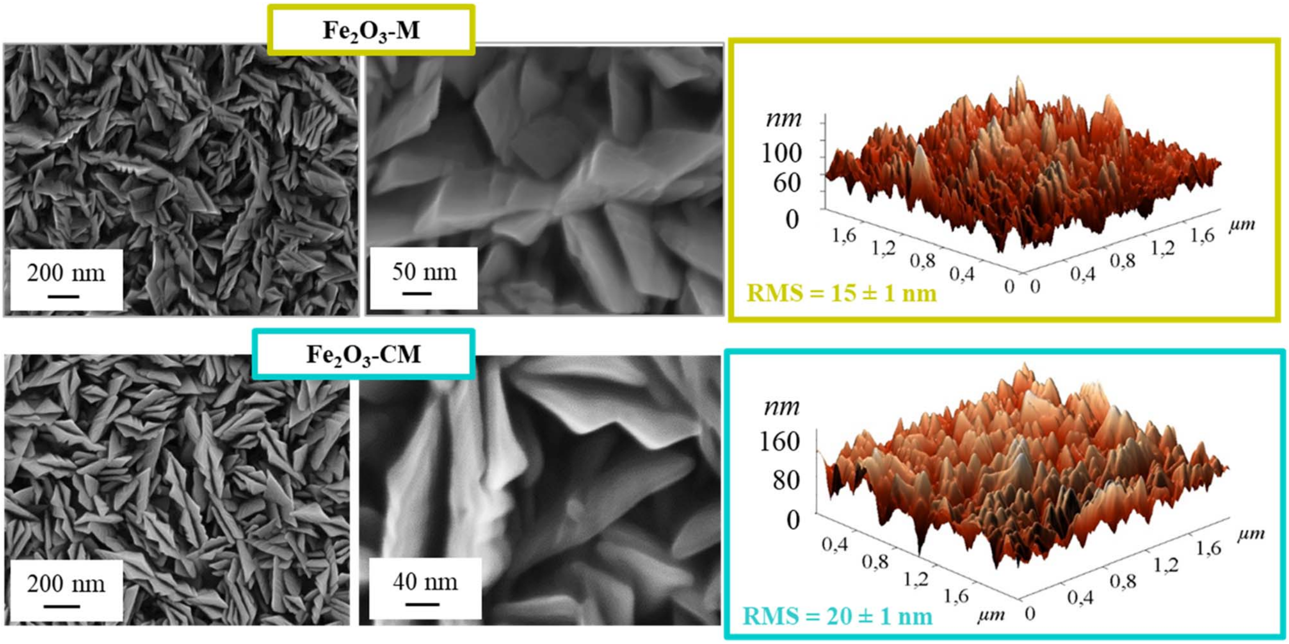

Fig. 1 Morphological characterization of $Fe_2O_3$ deposits functionalized with gCN(M) (top panel) and gCN(CM) (bottom panel): FE-SEM (left) and AFM micrographs (right).

$\mu m^2$ region and sampling secondary ions from a 7 × 7 $\mu m^2$ sub-area in order to avoid crater effects. The sputtering time was converted into depth based on the deposit thickness values measured by FE-SEM analyses. Transmission electron microscopy (TEM) including high-resolution TEM (HRTEM), bright-field scanning TEM (BF-STEM), high angle annular dark-field scanning TEM (HAADF-STEM), electron diffraction (ED), and EDXS elemental mapping were performed using a JEOL ARM200F cold FEG double aberration corrected microscope, equipped with a large-angle CENTURIO EDX detector, an Orius CCD camera, and a Quantum GIF. Electron energy loss spectroscopy (EELS) and additional EDXS measurements were performed using a Thermo Fisher Scientific Themis Z 80-300 microscope equipped with a spherical aberration corrector at the probe side, a SuperX G2 EDX spectrometer, and a Gatan Continuum 1065 electron energy loss spectrometer.

### 2.3 Electrochemical functional tests

Photoelectrocatalytic activity tests were performed at room temperature using an integrated system consisting of a Zennium-PRO and a PP212 unit from Zahner GmbH, coupled with an optical bench containing a Zahner photoelectrochemical cell (Fig. S1†). FTO-supported $Fe_2O_3$-gCN systems were used as working electrodes, whereas a Pt coil and a Ag/AgCl electrode were used as the counter and reference electrodes, respectively. Linear sweep voltammetry (LSV; scan rate = 5 mV $s^{-1}$) measurements were first performed in alkaline-simulated seawater (0.5 M KOH + 0.5 M NaCl),[20,40] and subsequently, in Adriatic seawater picked up at the seaside of Rosolina (RO), Italy. The latter was preliminarily treated by adding KOH and filtering the precipitate [mainly formed by $Mg(OH)_2$; final pH = 13.6].[20]

The overpotential ($\eta$) for the oxygen evolution reaction was calculated as follows:[20,25]

$$\eta\ (\mathrm{V}) = E_{\mathrm{RHE}} - 1.23 \tag{1}$$

where $E_{\mathrm{RHE}}$ and 1.23 are respectively the experimental potential and $E^\circ$ value for $O_2$ evolution, both on the reversible hydrogen electrode (RHE) scale. Tafel slopes were obtained by plotting the overpotential *vs.* RHE against log (current density).[20,22,24,41,75]

The applied bias photon-to-current efficiency (ABPE) (%) curves were obtained using the following equation:[42,75]

$$\mathrm{ABPE}\ (\%) = ([j \times (1.23 - E)]/P) \times 100 \tag{2}$$

where $j$ (mA $cm^{-2}$) is the photocurrent density at potential $E$ (V *vs.* RHE)), and $P$ is the incident light intensity (50 mW $cm^{-2}$, emitted from a white-light LED source), constantly measured by a photodiode in front of the cell. ABPE represents the photocurrent collected per incident photon, taking into account the external applied bias required relative to the water splitting voltage of 1.23 V.[76]

The incident photon-to-current conversion efficiency (IPCE) is a measure of the ratio of the photocurrent (converted to an electron transfer rate) *vs.* the rate of incident photons (converted from the calibrated power of a light source) as a function of wavelength. The IPCE (%) takes into account the efficiencies for photon absorption/charge excitation and separation ($\eta_{e^-/h^+}$), charge transport within the solid to the solid–liquid interface transport ($\eta_{\mathrm{transport}}$), and interfacial charge transfer across the solid–liquid interface ($\eta_{\mathrm{interface}}$).[76] The IPCE was measured in the potential interval 0.85–1.55 V *vs.* RHE, and the values were calculated as follows:[37,63]

$$\mathrm{IPCE}(\%) = \frac{(1240 \times j)}{(\lambda \times P)} \times 100 \tag{3}$$

where $j$ is the photocurrent density (mA cm$^{-2}$), $\lambda$ is the incident light wavelength (nm), and $P$ is the incident light power density for each wavelength. Measurements were obtained by using eight different LED light sources with wavelengths 365, 405, 447, 505, 590, 645, 735, and 810 nm. Each source light intensity was measured in real time by a photodiode during LSV acquisition.

Chronoamperometry (CA) analyses were carried out at 1.45 V (*vs.* RHE). Iodometric titration was used for the determination of hypochlorite species generated during OER (see ESI,† Section S-1.3).

Additional details on material preparation and characterization are reported in the ESI.†

# 3. Results and discussion

## 3.1 Material chemico-physical characterization

Preliminary attention was paid to the structural, optical and morphological characterization of $Fe_2O_3$ deposits (Fig. S2–S4† and related observations), based on which an optimal iron oxide growth temperature of 400 °C was identified, as indicated in Scheme 1. Under these conditions, an α-$Fe_2O_3$ (*hematite*) deposit with a porous lamellar structure and a thickness of 450 nm was obtained. After functionalization with gCN (Fig. 1), the system morphology did not undergo significant modifications with respect to bare iron(III) oxide. This evidence pinpointed that the adopted functionalization procedure was mild enough to maintain unaltered the original $Fe_2O_3$ nano-organization. EDXS analyses on $Fe_2O_3$-gCN systems (Fig. S5†) revealed an even distribution of both carbon and nitrogen over the whole analyzed areas, indicating a high lateral compositional homogeneity. AFM analyses (Fig. 1) yielded an enhanced roughness on passing from $Fe_2O_3$–M to $Fe_2O_3$–CM, suggesting a parallel increase of material active area, beneficial for the target application.[66]

X-ray diffraction (XRD) patterns of $Fe_2O_3$–M and $Fe_2O_3$–CM (Fig. S6a†) ruled out any significant structural variation after gCN introduction in comparison to the pristine iron(III) oxide. No signals due to graphitic carbon nitride could ever be detected, due to its low overall amount, as well as to its high dispersion into $Fe_2O_3$ (see below). Optical spectra (Fig. S6b†) evidenced an increased light harvesting of composite systems with respect to bare $Fe_2O_3$.

The corresponding band gap values (Fig. S6c†) were almost the same as those of pristine iron(III) oxide ($\approx$2.1 eV, compare Fig. S2†), $Fe_2O_3$ being the predominant system component. FE-SEM and EDXS results for the composite system after functionalization with CoPi are reported in Fig. S7† (see also related observations).

To investigate the composition and elemental chemical states of the target materials, XPS analyses were carried out (see also Fig. S8†). The C 1s signals resulted from the contribution of three distinct components (Fig. 2a, S9 and Table S1;† see also Fig. 2f): $C_0$, related to adventitious carbon;[35,45,55,62,66,77,78] $C_1$, ascribed to C–$NH_x$ groups ($x$ = 1 and 2) located on gCN heptazine ring edges;[2,52,62,66,75,77,79] $C_2$, due to N–C=N carbon atoms in the aromatic rings of the gCN framework.[37,43,48,54,58,59,62] As regards the N 1s photoelectron peaks (Fig. 2b, c, S10a and Table S2†), component $N_1$ was assigned to bi-coordinated nitrogen centres (C=N–C).[2,21,43,46,47,79] Signal $N_2$ corresponded to tertiary N atoms [N–(C)$_3$, $N_{3c}$] in the gCN network,[3,14,51,54,59,64] and signal $N_3$ was related to uncondensed -$NH_x$ groups[18,26,37,44,52,58,64,77] (compare also Fig. 2f). Upon going from the M-derived sample ($Fe_2O_3$–M) to CM-containing ones ($Fe_2O_3$–CM and $Fe_2O_3$–CM–CoPi), $N_3$ component contribution to the overall N 1s photopeak underwent a more than two-fold increase (Fig. 2e and Table S2†). The higher content of uncondensed amino groups in CM-derived systems highlighted their lower polymerization degree in comparison to melamine-derived samples.[66] As a matter of fact, an increased amino-group content can favourably influence the anchoring of carbon nitride to the underlying $Fe_2O_3$ deposits. Besides improving material stability, an important pre-requisite for practical end-uses, this issue can, in turn, promote charge transfer from gCN to $Fe_2O_3$ and directly affect the ultimate material activity (see below).[5] In fact, defects resulting from –$NH_x$ presence may act as hole capturing sites, suppressing the detrimental recombination processes of photogenerated electrons and holes.[5,66,75,79]

It is worthwhile noticing that BEs of components $C_1$ and $C_2$, as well as of the three bands contributing to the N 1s signal, show an increase in comparison to the reported values for bare gCN[18,26,31,32,48,60,63,77,78] (+0.2 eV, for $Fe_2O_3$–M, and + 0.3 eV, for $Fe_2O_3$–CM and $Fe_2O_3$–CM–CoPi; see Tables S1 and S2†). Such BE shifts reveal a strong $Fe_2O_3$-gCN interaction[3,14,43,53,54] due to the formation of $Fe_2O_3$/gCN heterojunctions,[49] with gCN → $Fe_2O_3$ interfacial electron transfer,[42,43] promoted by the intimate contact between the single system constituents. The slightly higher shift observed for CM-derived systems in comparison to the M-derived one (see BE values in Tables S1–S2†) suggested a more efficient charge transfer in the former case. These conclusions were supported by the analysis of Fe 2p photopeaks (Fig. 2d). In fact, for bare iron oxide, both the signal shape and its energy position confirmed that phase-pure $Fe_2O_3$ was obtained [see also Table S3;† BE (Fe 2p$_{3/2}$) = 711.2 eV; spin–orbit splitting (SOS) = 13.5 eV].[6,7,13,18,25,46,47,50,58] For composite $Fe_2O_3$-gCN systems, the Fe 2p position underwent a red shift, more marked for CM-derived specimens (corresponding to a BE decrease of −0.2 eV, for $Fe_2O_3$–M, and −0.3 eV, for $Fe_2O_3$–CM and $Fe_2O_3$–CM–CoPi). O 1s fitting results are reported in Fig. S11 and Table S4.†

Complementary information on material in-depth composition, with particular regard to gCN spatial distribution, was gained by SIMS profiling (Fig. 3). For all the investigated systems, oxygen ionic yield did not undergo remarkable variations as a function of depth. The parallel Fe and O signal trends highlighted their common chemical origin, in line with the presence of iron(III) oxide as the predominant system component. The tailing of tin signals into the deposits was ascribed to Sn diffusion

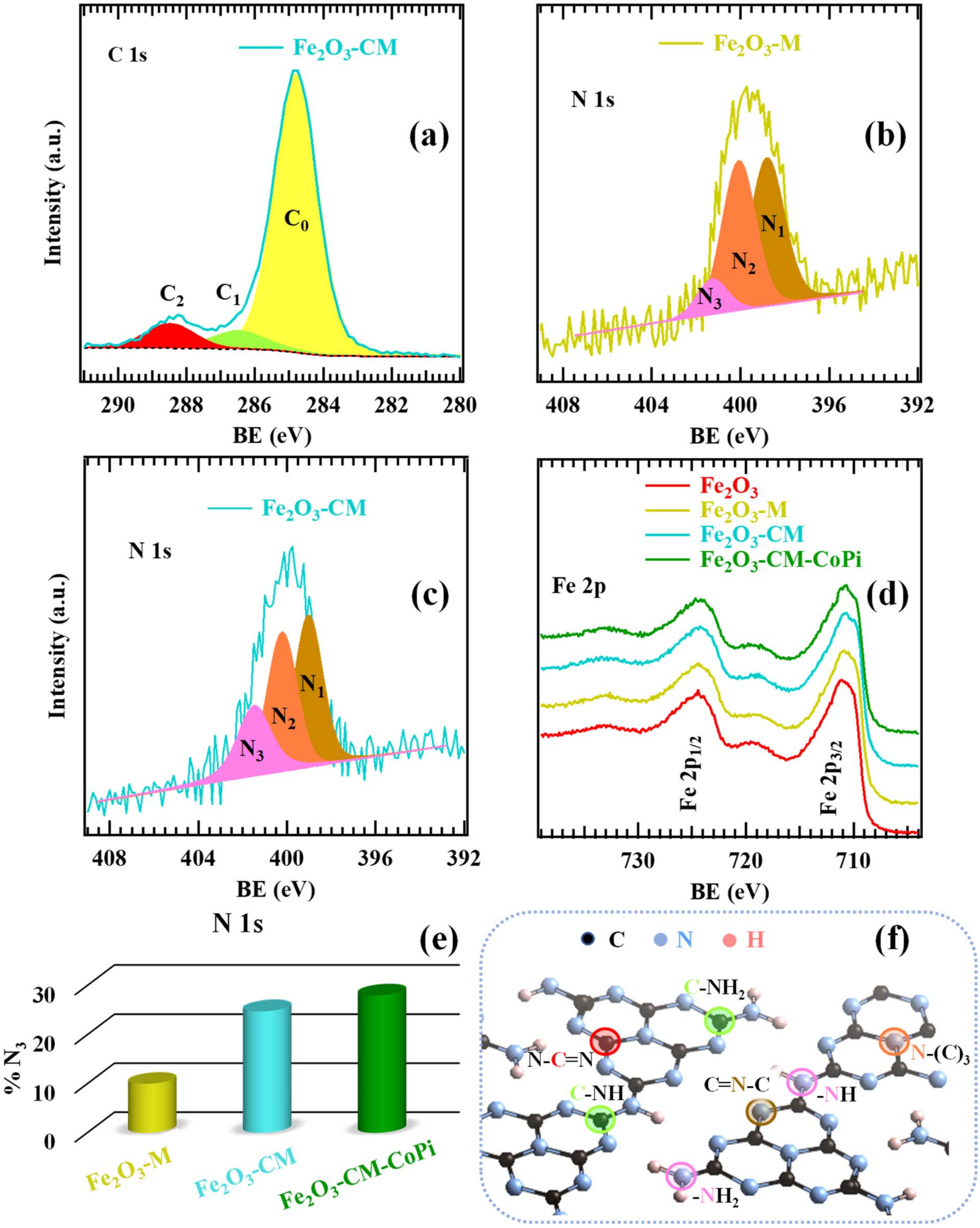

Fig. 2 XPS surface characterization: C 1s (a), N 1s (b and c) and Fe 2p (d) photoelectron peaks for $Fe_2O_3$–M and $Fe_2O_3$–CM specimens. In panel (d), signals pertaining to bare $Fe_2O_3$ and to $Fe_2O_3$–CM functionalized with CoPi are also reported for comparison. (e) Percentage contribution of the $N_3$ component (related to amino groups) to the overall N 1s signal for the investigated samples. (f) Sketch of graphitic carbon nitride structure,[66,75] in which non-equivalent carbon and nitrogen sites are marked. Color codes are the same as in panels (a–c), in Fig. S9 and S10, and in Tables S1, S2†.

from the FTO substrate promoted by thermal treatment. This phenomenon, already observed in previous studies, might result in an improved electrical conductivity, favourably affect the ultimate material performances.[6,7,20] The similarity between carbon and nitrogen ionic profiles revealed that the predominant contribution to the C signal arose from gCN presence, rather than

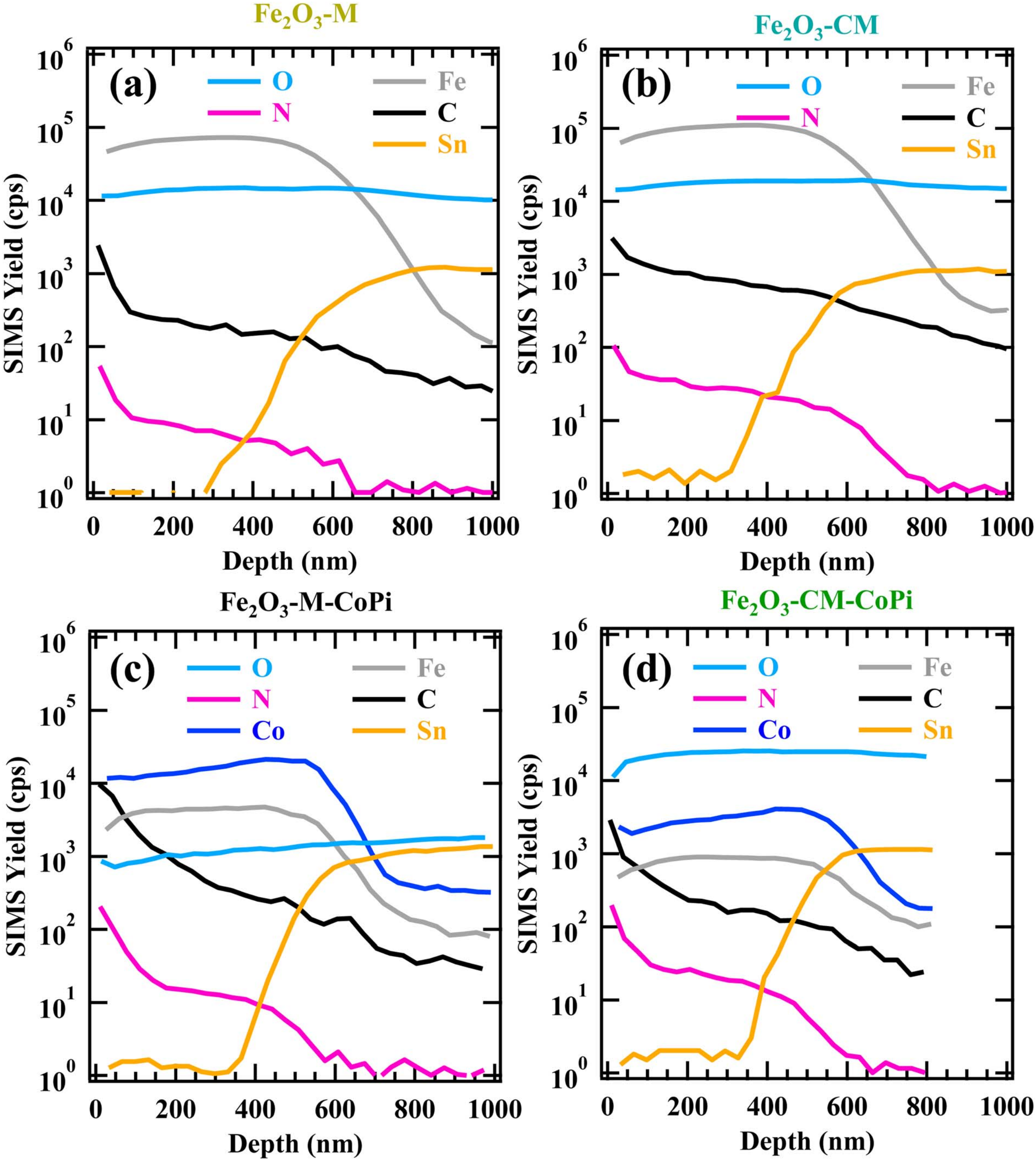

Fig. 3 SIMS depth profiles of specimens: $Fe_2O_3$–M (a), $Fe_2O_3$–CM (b), $Fe_2O_3$–M–CoPi (c), and $Fe_2O_3$–CM–CoPi (d).

from adventitious contamination. Indeed, the trends of C and N ionic yields as a function of depth suggested the presence of gCN throughout the entire $Fe_2O_3$ deposits. This result, related, in turn, to the iron(III) oxide open morphology (see Fig. 1 and S4† and pertaining observations), evidenced an intimate contact between the system components, of key importance for the target functional applications. A careful inspection of the profiles reported in Fig. 3 revealed that the outermost material region was gCN-rich, a phenomenon more evident for $Fe_2O_3$–M and $Fe_2O_3$–M–CoPi (Fig. 3b and d). Conversely, this effect was less marked for CM-derived specimens, indicating a good dispersion of gCN into the underlying $Fe_2O_3$. The resulting enhanced $Fe_2O_3$/gCN contact can boost the system activity due to the higher density of heterojunctions (see below).[20] After CoPi introduction, Fe and Co profiles presented a close resemblance (Fig. 3c and d). In particular, for specimens $Fe_2O_3$–M–CoPi and $Fe_2O_3$–CM–CoPi, Co content was similar within an uncertainty of ±6%, and CoPi distribution was uniform within ±3%. The latter result might synergistically contribute to an additional performance improvement (see below).

To shed light into the system nanostructure, efforts were dedicated to a detailed characterization by TEM and related techniques. In particular, ED, HRTEM, and HAADF-STEM were used for phase identification, whereas complementary information on the composition and electronic structure at the nanoscale was gained by EDXS and EELS analyses. Fig. 4 displays the TEM results obtained for specimen $Fe_2O_3$–CM. The $\alpha$-$Fe_2O_3$ deposit exhibited a columnar structure (Fig. 4a; typical grain size $= 50 \div 70$ nm; overall thickness $\approx$450 nm). Similar features were exhibited even by sample $Fe_2O_3$–M (see also Fig. S12†). Low-magnification cross-section HAADF-STEM and BF-STEM images, together with EDXS-STEM elemental maps (Fig. 4a), did not clearly show gCN presence. Nevertheless, the dark contrast on the grain surface (see Fig. 4c) suggested the formation of a very thin gCN layer. In fact, integration of EDXS signals over the whole sample thickness (Fig. 4b) revealed the occurrence of carbon and nitrogen signals. These results confirmed the faceted structure of hematite grains, in line with the FE-SEM results (see above), along with a uniform gCN distribution over iron oxide surface. These outcomes, together with XPS and SIMS ones (see above), point out to the presence of an ultrathin gCN layer covering the underlying iron oxide, a favourable feature to maximize interfacial $Fe_2O_3$/gCN interactions and promote hole migration to the gCN surface for water oxidation.[80]

The HRTEM characterization of iron(III) oxide is reported for sample $Fe_2O_3$–CM in Fig. 4c, whereas Fig. 4d displays the corresponding SAED pattern. The latter is in full agreement with the hexagonal $\alpha$-$Fe_2O_3$ structure (space group: $R\bar{3}c$ (167); $a = 0.5035$ nm, $c = 1.3747$ nm), in line with XRD results (see Fig. S2†). The observed crystalline grains appear free from any defect. Such material characteristics, along with the columnar structure and nanosized morphology of the iron oxide deposit, are expected to be beneficial for photoelectrochemical applications.[71,81] $Fe_2O_3$ presence was further confirmed by EELS analyses (Fig. 4e), exhibiting an optimal match with reference $\alpha$-$Fe_2O_3$ regarding both O K and Fe $L_{2,3}$ features and the overall spectral shape.[82]

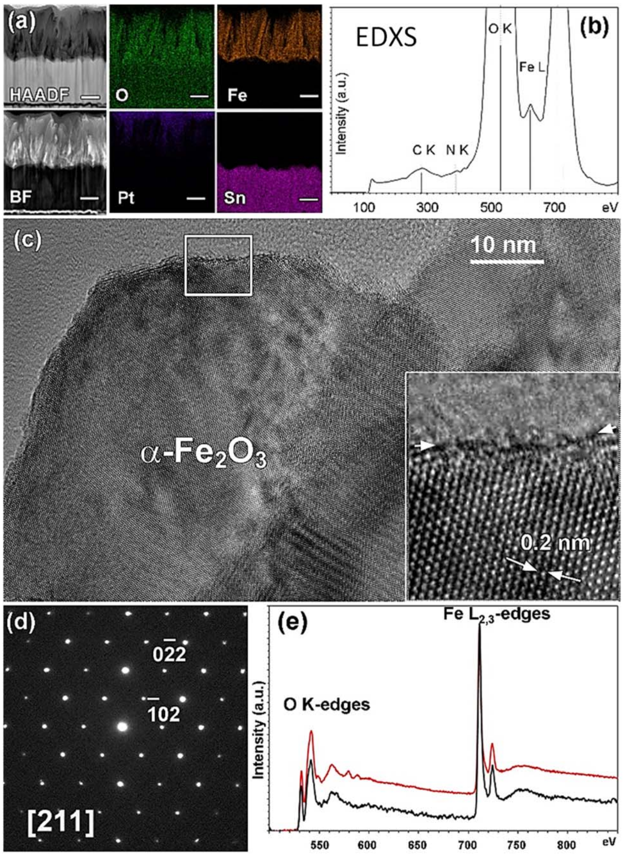

Fig. 4 (a) Cross-section HAADF-STEM, BF-STEM images and EDXS-STEM elemental maps for O K, Fe K, Pt M, and Sn L collected on sample $Fe_2O_3$–CM. Scale bar is 200 nm. (b) EDXS spectra integrated over the full thickness of the iron oxide deposit. (c) Bright field [211] HRTEM image of an $\alpha$-$Fe_2O_3$ single grain. A magnified image of the region framed by the white box is shown in the inset, where white arrows indicate $\alpha$-$Fe_2O_3$ interplanar spacing. (d) SAED pattern corresponding to the above HRTEM image, indexed based on $Fe_2O_3$ hexagonal structure (ICSD 40142). (e) Integrated EELS spectrum (black) and $\alpha$-$Fe_2O_3$ reference spectrum (red).[83]

### 3.2 Electrochemical characterization

Fig. 5 reports the most relevant electrochemical results for the target samples, acquired in simulated seawater. As far as LSV curves are concerned (Fig. 5a), all specimens featured modest current density values in the darkness. In a different way, upon illumination a systematic current density increase took place, accompanied by a significant decrease in onset potential values. As can be observed, OER performances under irradiation improved upon gCN introduction, and further increased when $Fe_2O_3$-gCN composites were decorated with CoPi. The actual photoelectrocatalytic performances (Tables S5 and S6†) are in line, or even better, than those exhibited in saline/seawater splitting by other $Fe_2O_3$- or gCN-containing electrocatalysts (compared with literature results summarized in Tables S7 and S8†). As can be observed in Fig. 5a and Table S5,† both composites yielded current density values higher than those of bare $Fe_2O_3$, revealing that even small gCN amounts are sufficient to boost the photoelectrocatalytic activity. In particular, the functional performances of $Fe_2O_3$–CM-based materials were systematically better than those of $Fe_2O_3$–M ones.

The observed improvement can be mainly ascribed to the electronic interplay occurring at the $Fe_2O_3$/gCN interface. In particular, as sketched in Fig. 6, charge transfer across $Fe_2O_3$/gCN interfaces occurs due to a staggered type-II heterojunction mechanism,[13] at variance with literature reports on $\alpha$-$Fe_2O_3$/gCN photocatalysts, for which a *Z*-scheme junction has been reported.[2–4,17–19,42,47–49,51–54,58,60,64] As can be observed in Fig. 6, upon irradiation, valence-to-conduction band electron excitation occurs. Thanks also to the intimate $Fe_2O_3$/gCN contact, as revealed by SIMS and TEM data (see above),[45] electrons from the more negative gCN conduction band are transferred to the less negative $Fe_2O_3$ one, whereas holes flow from the $Fe_2O_3$ valence band to the gCN one, thus yielding enhanced electron–hole separation.[43,46,57,84] Subsequently, under the action of the applied bias voltage, electrons in the $Fe_2O_3$ conduction band are

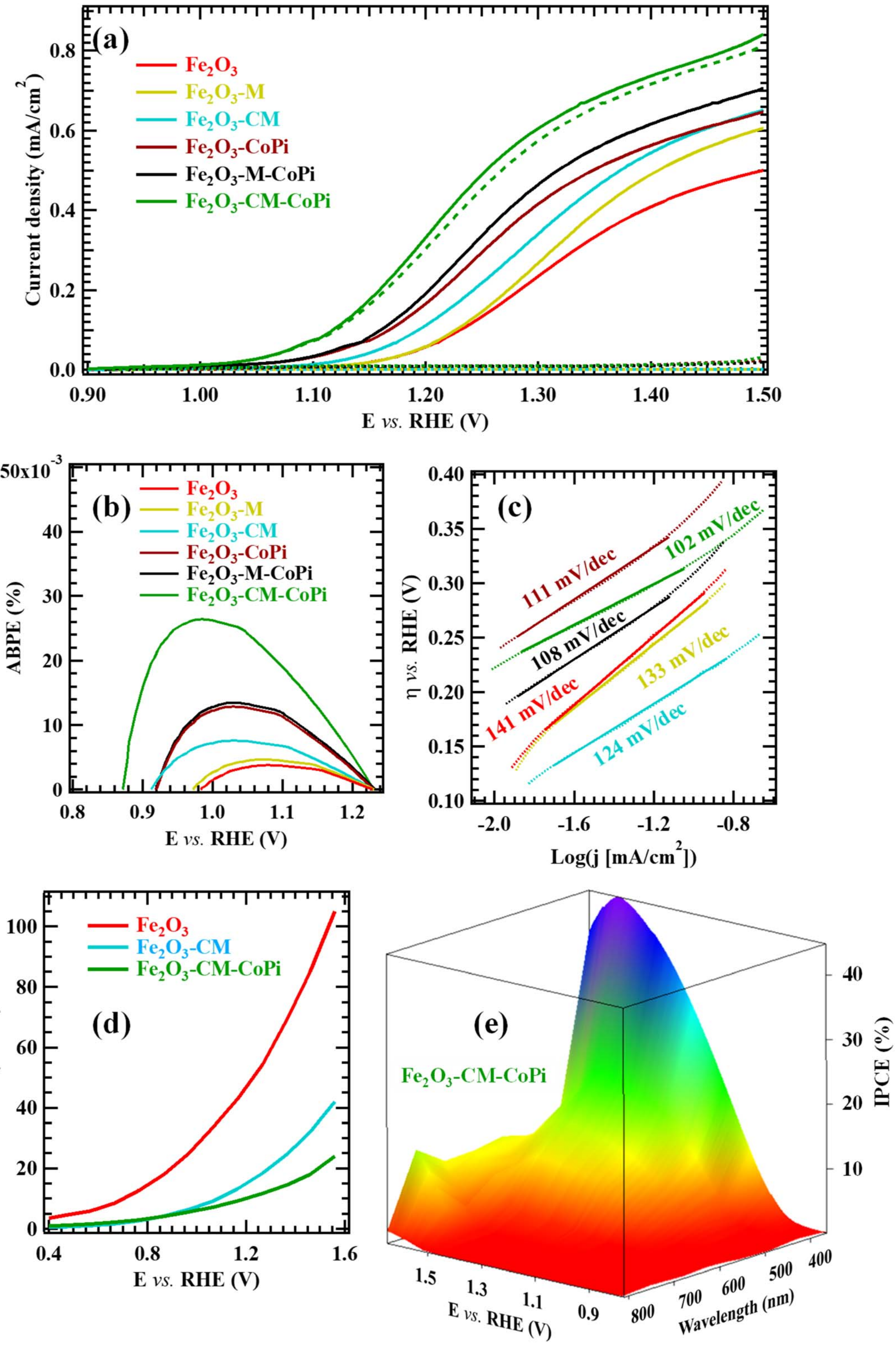

**Fig. 5** OER performances of $Fe_2O_3$ and $Fe_2O_3$-gCN electrodes, both as such and functionalized with CoPi, in simulated alkaline seawater. (a) iR-corrected LSV scans under illumination and in the darkness (continuous and dotted lines, respectively). For the best performing $Fe_2O_3$–CM–CoPi sample, the iR-uncorrected curve under irradiation is also displayed as dashed lines. As a general rule, the photocurrent difference between iR-corrected and uncorrected scans was lower than ≈4–5% for bias values below 1.5 V *vs.* RHE. (b) ABPE (%) curves. (c) Tafel plots. Dashed and continuous lines indicate experimental and fitting curves, respectively. (d) Mott–Schottky plots *vs.* the applied potential for selected specimens (acquired at 1 kHz). (e) IPCE (%) spectra for sample $Fe_2O_3$–CM–CoPi.

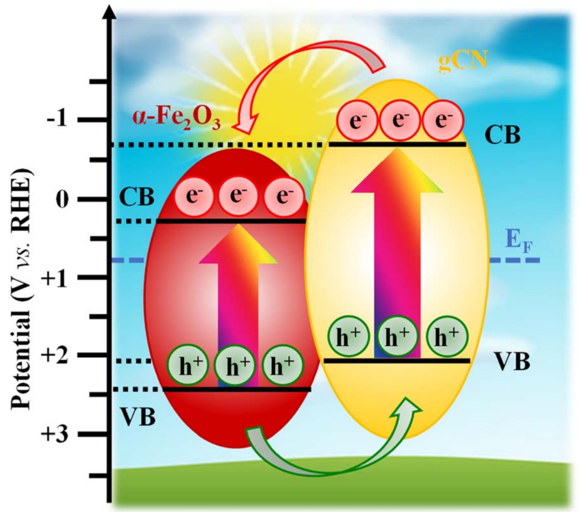

Fig. 6 Representation of the interfacial band structure at the carbon nitride/$Fe_2O_3$ heterojunction.[5,20,26,43,56,57,59,66] CB and VB mark the conduction and valence band edges, respectively. VB and CB energy levels related to gCN and $Fe_2O_3$ have been obtained by photoelectron spectroscopy measurements (Fig. S13†) and optical band gap values. The optical band gap value for $Fe_2O_3$ is reported in Fig. S3,† while the ones for gCN(M) and gCN(CM) are referred to published data.[66] The marked Fermi level energy ($E_F$) has been obtained by Mott–Schottky analyses (see Section S-1.3†).

injected in the external circuit through the FTO substrate[34] and are transported towards the cathode, while holes are progressively accumulated at gCN sites, where water is directly oxidized to $O_2$. Consequently, electrons and holes participate in hydrogen evolution reaction (HER) and OER, respectively. Owing to this type-II configuration, charge carrier recombination is suppressed and their extraction and utilization can be significantly improved, leading to superior photoelectrocatalytic performances of nanocomposite systems in comparison to their single-phase counterparts.

At this stage, the question to be answered is: why do gCN(CM)-derived systems exhibit better performances with respect to the homologous M-derived ones? The reasons accounting for this phenomenon are: (i) the higher content of defects related to amino-group presence (see XPS data) and (ii) the more homogeneous in-depth dispersion of gCN(CM) into $Fe_2O_3$ in comparison to gCN(M) (compare SIMS results in Fig. 3), resulting in a more efficient $Fe_2O_3$/gCN contact and improved separation of photogenerated electrons and holes.[66] In fact, ABPE profiles[76] (Fig. 5b) indicate that $Fe_2O_3$–CM specimens are more efficient with respect to bare $Fe_2O_3$ and $Fe_2O_3$–M ones. Furthermore, samples decorated with CoPi particles show higher ABPE values than the corresponding CoPi-free ones, with $Fe_2O_3$–CM–CoPi yielding the best performances. An additional figure of merit to assess the material activity, with particular regard to the electrode reaction kinetics,[20–22,25,41] is the Tafel slope. In the case of OER, for which low overpotentials are needed, lower Tafel slopes are highly desirable. In this regard, Fig. 5c reveals that the decoration of $Fe_2O_3$-gCN composites with CoPi further improves the OER kinetics. Moreover, all samples functionalized with gCN(CM) are characterized by lower Tafel slopes in comparison to gCN(M)-containing ones.

Altogether, data reported in Fig. 5a–c indicate that the best performing photoanode is $Fe_2O_3$–CM–CoPi. The same conclusion is corroborated by a comparative examination of results obtained from Mott–Schottky analyses (see Fig. 5d and S15†). In fact, Table S9† indicates a negative shift of the flat band potential ($V_{FB}$; see Section S-1.3†) upon going from $Fe_2O_3$, to $Fe_2O_3$–M, to $Fe_2O_3$–CM, accompanied by a parallel increase in charge carrier concentration ($N_D$). An analogous trend is exhibited by CoPi-functionalized samples, which feature systematically lower (higher) $V_{FB}$ ($N_D$) values with respect to the previous ones. Since a deeper $V_{FB}$ (*i.e.*, a deeper Fermi level energy) allows us to achieve the OER onset using a lower bias, $Fe_2O_3$–CM–CoPi is confirmed to be the best performing system among the investigated ones. The corresponding IPCE analysis (Fig. 5e) yielded a value of ≈40% at 1.6 V *vs.* RHE (compare also with Fig. S16†).

Subsequently, the electrochemical activity of CoPi-decorated specimens was also tested in real alkaline seawater. Fig. 7a displays the related LSV curves for specimens $Fe_2O_3$–CoPi, $Fe_2O_3$–M–CoPi, and $Fe_2O_3$–CM–CoPi. The above observed activity trend was still maintained, though the obtained photocurrent density values were appreciably lower than those reported in Fig. 5a, due to the different electrolyte composition.[85] ABPE curves (Fig. 7b) and Tafel slopes (Fig. 7d) present an analogous trend. Taken together, these data suggest the occurrence of a cooperative effect between the type-II $Fe_2O_3$/gCN junction (see Fig. 6) and the CoPi electrocatalytic activity.[86] In this regard, as already mentioned, the accumulation of electrons and holes in $Fe_2O_3$ CB and gCN VB, respectively, suppresses $e^-/h^+$ recombination at low biases, thus improving the charge injection efficiency. The introduction of CoPi particles and their electrocatalytic action towards OER[87] result in favorable improvement of the overall performances.[86] It is also important highlighting that seawater electrolysis led to a very modest $ClO^-$ production, as can be deduced from Fig. 7c, comparing two beakers containing seawater after electrolysis for 1 h (left) and a $1.0 \times 10^{-7}$ M $ClO^-$ solution (right) after KI introduction in both cases (see Section S-1.3† for further details).

The time stability of CoPi-containing $Fe_2O_3$ and $Fe_2O_3$-gCN samples was tested by CA measurements at 1.45 V *vs.* RHE (Fig. 7e–f). As far as prolonged CA experiments are concerned (Fig. 7f), for pristine $Fe_2O_3$–CoPi a current density loss of ≈26% took place after 15 h of operation, and the presence of carbon nitride, in spite of its low amount, afforded a very favorable stability improvement (for $Fe_2O_3$–M–CoPi and $Fe_2O_3$–CM–CoPi, $j$ losses of ≈14 and ≈4% respectively). The very limited photocurrent density decrease observed for $Fe_2O_3$–CM–CoPi was comparable, or lower, than those reported in analogous seawater splitting tests for various gCN or $Fe_2O_3$-based electrocatalysts (namely, Ru,Ni-doped $Fe_2O_3$,[41] NiFe layered double hydroxides (LDH)/Mo-doped g-$C_3N_4$,[21] and $Fe_2O_3$/NiO on Ni-foams[24]), as well as for $NiO_x$-$FeO_x$@g-$C_3N_4$,[22] $TiO_2$@g-$C_3N_4$–CoPi,[37] $WO_3$@g-$C_3N_4$,[63] and $In_2S_3$–$C_3N_4$[88] photoelectrocatalysts. A similar result, far from being straightforward especially upon

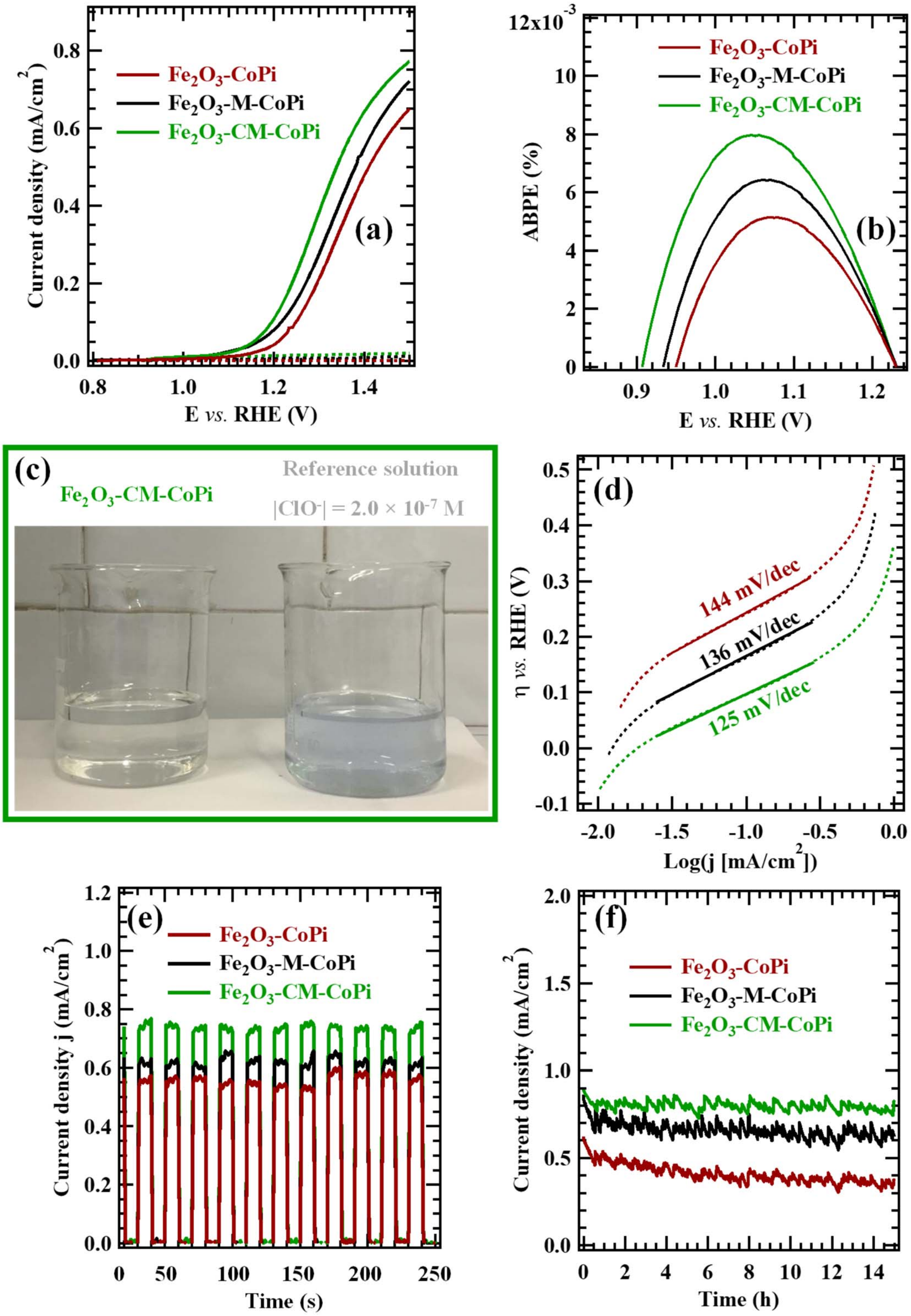

Fig. 7 Electrochemical OER performances of $Fe_2O_3$ and $Fe_2O_3$-gCN electrodes functionalized with CoPi in Adriatic alkaline seawater. (a) LSV curves under illumination and in the darkness (continuous and dashed lines, respectively). (b) ABPE (%) curves. (c) Photographs taken upon iodometric titration of OER solutions, showing a negligible $ClO^-$ formation in the case of $Fe_2O_3$–CM–CoPi. (d) Tafel plots. Dashed and continuous lines indicate experimental and fitting curves, respectively. (e) Chopped CA tests and (f) prolonged CA measurements, both at 1.45 V *vs.* RHE.

using seawater as electrolyte, emphasizes the applicative potential of the developed nanocomposites in the framework of an improved sustainability.

Additional information on the charge transfer processes occurring in the target systems was gained by IMPS analyses (ESI, Section S-2.3 and Fig. S17†). The synergistic action of gCN and CoPi in boosting functional performances is evidenced by the comparison of data acquired for $Fe_2O_3$–CoPi, $Fe_2O_3$–M–CoPi and $Fe_2O_3$–CM–CoPi samples before electrochemical testing in seawater. The kinetic constants and normalized IMPS Nyquist plots (Fig. S18†) indicate that the co-presence of gCN and CoPi is very effective in decreasing the recombination rate constants[89] ($k_{rec}$), yielding lower values than those measured for $Fe_2O_3$–CoPi. In a different way, charge injection constants ($k_{inj}$) present an increasing trend up to 1.00–1.05 V. gCN-containing samples are characterized by the highest $k_{inj}$ values and best charge injection efficiencies (Fig. S18†).

Fig. 8 reports the results obtained from IMPS analysis after electrochemical testing in seawater. The $k_{inj}$ *vs.* potential trend (Fig. 8a; see also Fig. S18a†) suggests, at least for $Fe_2O_3$–CoPi, a Fermi level pinning caused by surface states at the material/electrolyte interface, where holes are accumulated.[70,90,91] In a different way, for both $Fe_2O_3$–M–CoPi and $Fe_2O_3$–CM–CoPi, these surface states are passivated by the remaining CoPi particles,[92,93] which extract photogenerated holes. Co(II) centers can, in fact, easily trap holes on the oxide surface.[91] In this regard, the recombination frequency is also reduced by the presence of a type-II $Fe_2O_3$/gCN junction, since $k_{rec}$ values for $Fe_2O_3$–M–CoPi and $Fe_2O_3$–CM–CoPi samples are appreciably lower than those for $Fe_2O_3$–CoPi in the whole potential range.[13] The introduction of CoPi also leads to an increase in $k_{inj}$ values up to ≈ 1.1 V, in line with previous results.[89] Interestingly, the $k_{inj}$ values for $Fe_2O_3$–M–CoPi and $Fe_2O_3$–CM–CoPi are higher than those found for $Fe_2O_3$–CoPi only at low potentials, whereas a decrease is observed at biases higher than 1.1 V (Fig. 8a). This $k_{inj}$ behaviour can be related to a progressive change in the OER mechanism as

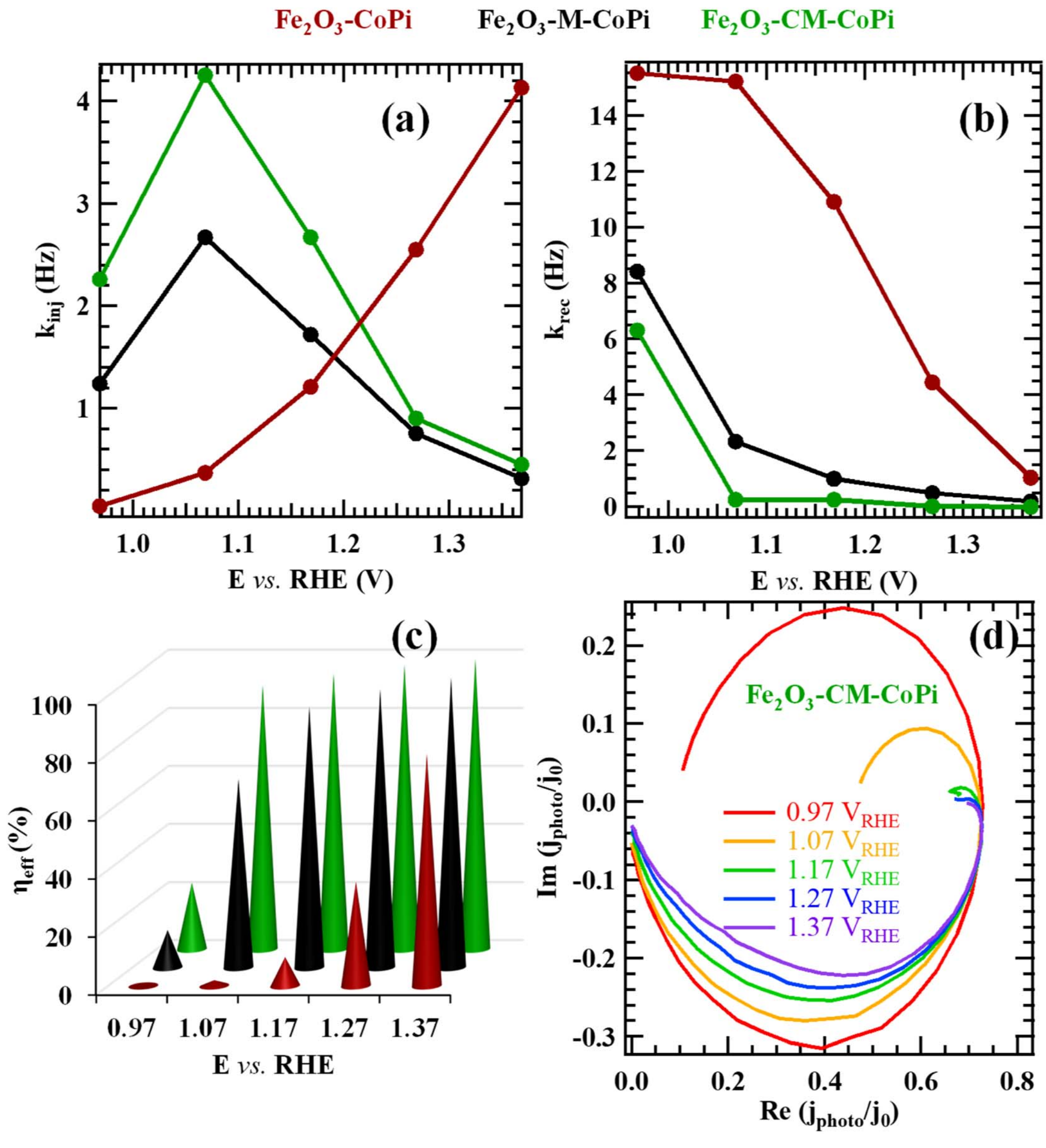

Fig. 8 (a) $k_{inj}$, (b) $k_{rec}$, and (c) charge transfer efficiency [$\eta_{eff} = k_{inj}/(k_{rec} + k_{inj})$] values obtained from IMPS experiments performed after photoelectrochemical work in seawater for $Fe_2O_3$–CoPi, $Fe_2O_3$–M–CoPi and $Fe_2O_3$–CM–CoPi. (d) Normalized Nyquist plots of IMPS data for $Fe_2O_3$–CM–CoPi. The corresponding plots for $Fe_2O_3$–CoPi and $Fe_2O_3$–M–CoPi are reported in Fig. S19.†

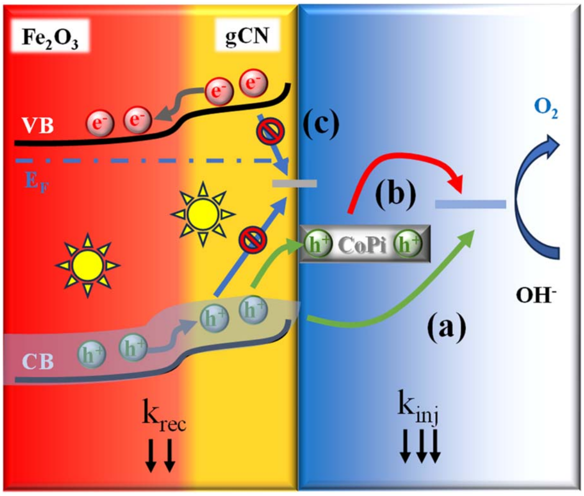

Fig. 9 Simplified model of the elementary processes taking place on the $Fe_2O_3$-gCN photoanode in the presence of CoPi. Photoexcited carriers move towards the semiconductor/electrolyte interface with direct water oxidation by VB holes (a), and charge transfer *via* a CoPi co-catalyst (b). Surface state-mediated recombination is appreciably depressed (c).

the bias is increased, from direct water oxidation at the $Fe_2O_3$/gCN surface to oxidation *via* CoPi. Such a phenomenon can be explained considering that the exposed $Fe_2O_3$/gCN surface can no longer keep up with the increasing flux of photogenerated holes and, therefore, a higher hole fraction will oxidize CoPi as the potential is increased. As a result, a decrease in $k_{inj}$ values occurs upon increasing the applied potential. Overall, these data indicate the presence of two paths for OER: direct injection of holes from gCN VB or, for potentials higher than ≈1.1 V, injection through CoPi particles (Fig. 9).

Importantly, the good performances of gCN-containing samples are not appreciably deteriorated by the action of seawater in comparison with the freshly prepared ones. This conclusion was also testified by post-*operando* XPS analyses on $Fe_2O_3$–M and $Fe_2O_3$–CM, enabling us to rule out any significant dissolution/degradation upon photoelectrochemical testing (see Fig. S20 and S21†; compare with Fig. 2 and S9–S11†). In fact, none of the relevant photopeaks showed any appreciable difference with respect to the original situation, and even quantitative analyses were very similar to those of freshly prepared samples (Fig. S22†). In excellent agreement with these outcomes, XRD and FE-SEM analyses yielded results very similar to the ones related to freshly prepared materials (compare Fig. S6a with Fig. S23, and Fig. S7a–d with Fig. S24†).

## 4. Conclusions

In summary, this work has been focused on the development of eco-friendly photoanodes for seawater splitting based on iron(III) oxide and graphitic carbon nitride. After the plasma-enhanced chemical vapor deposition of $Fe_2O_3$ onto FTO substrates, the systems were functionalized with gCN by electrophoresis, annealed in air, and eventually decorated with CoPi particles. Material structure–property interplay was elucidated by a multi-technique investigation using complementary analytical tools, among which IMPS provided valuable mechanistic insights into the photocharge dynamics. The proposed synthesis route was found to be very versatile for the fabrication of $Fe_2O_3$-gCN nanocomposites with controllable morphology, tailored surface defectivity, and an intimate $Fe_2O_3$/gCN interfacial contact. After decoration with CoPi, the most appealing material featured a Tafel slope of ≈ 100 mV $dec^{-1}$ and overpotentials lower than the $ClO^-$ formation onset. In addition, photocurrent density values at 1.23 V *vs.* RHE showed a nearly 7-fold increase upon $Fe_2O_3$ functionalization with gCN and CoPi.

The present photoelectrocatalytic activities were rationalized based on the formation of staggered type-II $Fe_2O_3$/gCN heterojunctions, coupled with CoPi as a passivating co-catalyst, promoting the transfer and separation of photogenerated electron–hole pairs. This favourable behaviour was accompanied by an appreciable selectivity towards $O_2$ evolution, which, along with the remarkable material durability in alkaline environments, makes the obtained systems promising candidates for use as green, low-cost and robust electrodes for seawater splitting under solar illumination.

The present study demonstrated the importance of nanostructure engineering to develop photoanodes for the sustainable and efficient conversion of sunlight into chemical energy. These issues are of key importance to utilize water resources properly, alleviating energy shortage and environmental issues. Additional perspectives for a future sustainable development may concern the use of the present materials as photocatalysts for simultaneous water purification and energy generation, enabling us to conveniently transform wastes into resources under ambient conditions.

## Author contributions

Mattia Benedet: investigation, writing-reviewing and editing. Gian Andrea Rizzi: methodology, conceptualization and investigation. Oleg I. Lebedev and Vladimir Roddatis: investigation and data curation. Cinzia Sada: methodology, data curation, writing – reviewing, and editing. Jan-Lucas Wree and Anjana Devi: methodology, investigation, data curation, writing-original draft preparation. Chiara Maccato: conceptualization, writing-original draft preparation, writing – reviewing, and editing, supervision and resources. Alberto Gasparotto: methodology, investigation, data curation, writing-reviewing and editing. Davide Barreca: methodology, investigation, supervision and resources, writing – reviewing and editing. All authors contributed to the data acquisition, discussed the results, and commented on the manuscript.

## Conflicts of interest

There are no conflicts to declare.

## Acknowledgements

This research was funded by Progetti di Ricerca @CNR – avviso 2020 – ASSIST), Padova University (P-DiSC#04BIRD2020-UNIPD

EUREKA, DOR 2021–2023), and INSTM Consortium (INSTM21PDGASPAROTTO-NANO$^{MAT}$, INSTM21PDBARMACATENA). The authors are grateful to Dr A. Banzato for technical support. V. R. thanks the European Regional Development Fund and the State of Brandenburg for the Themis Z TEM (part of PISA). We also thank A. Schreiber (GFZ) for her help with FIB specimen preparation.

## References

1 C. Huang, Q. Zhou, D. Duan, L. Yu, W. Zhang, Z. Wang, J. Liu, B. Peng, P. An, J. Zhang, L. Li, J. Yu and Y. Yu, *Energy Environ. Sci.*, 2022, **15**, 4647–4658.
2 S. A. Hassanzadeh-Tabrizi, C.-C. Nguyen and T.-O. Do, *Appl. Surf. Sci.*, 2019, **489**, 741–754.
3 Q. Xu, B. Zhu, C. Jiang, B. Cheng and J. Yu, *Sol. RRL*, 2018, **2**, 1800006.
4 C. Zhao, M. Zheng, D. Wang, Q. Li and B. Jiang, *Energy Technol.*, 2020, **8**, 2000108.
5 X. Zou, Z. Sun and Y. H. Hu, *J. Mater. Chem. A*, 2020, **8**, 21474–21502.
6 D. Barreca, G. Carraro, A. Gasparotto, C. Maccato, M. E. A. Warwick, K. Kaunisto, C. Sada, S. Turner, Y. Gönüllü, T.-P. Ruoko, L. Borgese, E. Bontempi, G. Van Tendeloo, H. Lemmetyinen and S. Mathur, *Adv. Mater. Interfaces*, 2015, **2**, 1500313.
7 G. Carraro, C. Maccato, A. Gasparotto, K. Kaunisto, C. Sada and D. Barreca, *Plasma Processes Polym.*, 2016, **13**, 191–200.
8 A. Pei, R. Xie, Y. Zhang, Y. Feng, W. Wang, S. Zhang, Z. Huang, L. Zhu, G. Chai, Z. Yang, Q. Gao, H. Ye, C. Shang, B. H. Chen and Z. Guo, *Energy Environ. Sci.*, 2023, **16**, 1035–1048.
9 W. Tong, M. Forster, F. Dionigi, S. Dresp, R. Sadeghi Erami, P. Strasser, A. J. Cowan and P. Farràs, *Nat. Energy*, 2020, **5**, 367–377.
10 J. Juodkazytė, B. Šebeka, I. Savickaja, M. Petrulevičienė, S. Butkutė, V. Jasulaitienė, A. Selskis and R. Ramanauskas, *Int. J. Hydrogen Energy*, 2019, **44**, 5929–5939.
11 Y. Yao, X. Gao and X. Meng, *Int. J. Hydrogen Energy*, 2021, **46**, 9087–9100.
12 O. Alduhaish, M. Ubaidullah, A. M. Al-Enizi, N. Alhokbany, S. M. Alshehri and J. Ahmed, *Sci. Rep.*, 2019, **9**, 14139.
13 N. A. Arzaee, M. F. Mohamad Noh, N. S. H. Mohd Ita, N. A. Mohamed, S. N. F. Mohd Nasir, I. N. Nawas Mumthas, A. F. Ismail and M. A. Mat Teridi, *Dalton Trans.*, 2020, **49**, 11317–11328.
14 L. Kong, J. Yan, P. Li and S. F. Liu, *ACS Sustainable Chem. Eng.*, 2018, **6**, 10436–10444.
15 M. Mishra and D.-M. Chun, *Appl. Catal., A*, 2015, **498**, 126–141.
16 P. Sharma, J.-W. Jang and J. S. Lee, *ChemCatChem*, 2019, **11**, 157–179.
17 X. She, J. Wu, H. Xu, J. Zhong, Y. Wang, Y. Song, K. Nie, Y. Liu, Y. Yang, M.-T. F. Rodrigues, R. Vajtai, J. Lou, D. Du, H. Li and P. M. Ajayan, *Adv. Energy Mater.*, 2017, **7**, 1700025.
18 Y. Li, S. Zhu, Y. Liang, Z. Li, S. Wu, C. Chang, S. Luo and Z. Cui, *Mater. Des.*, 2020, **196**, 109191.
19 V. D. Dang, T. Annadurai, A. P. Khedulkar, J.-Y. Lin, J. Adorna, W.-J. Yu, B. Pandit, T. V. Huynh and R.-A. Doong, *Appl. Catal., B*, 2023, **320**, 121928.
20 L. Bigiani, D. Barreca, A. Gasparotto, T. Andreu, J. Verbeeck, C. Sada, E. Modin, O. I. Lebedev, J. R. Morante and C. Maccato, *Appl. Catal., B*, 2021, **284**, 119684.
21 Y. Du, Y. Zhang, X. Pu, X. Fu, X. Li, L. Bai, Y. Chen and J. Qian, *Chemosphere*, 2023, **312**, 137203.
22 T. u. Haq and Y. Haik, *ACS Sustainable Chem. Eng.*, 2022, **10**, 6622–6632.
23 Y. Kumar, R. Kumar, P. Raizada, A. A. P. Khan, A. Singh, Q. V. Le, V.-H. Nguyen, R. Selvasembian, S. Thakur and P. Singh, *J. Environ. Chem. Eng.*, 2022, **10**, 107427.
24 L. Li, G. Zhang, B. Wang, D. Zhu, D. Liu, Y. Liu and S. Yang, *ACS Appl. Mater. Interfaces*, 2021, **13**, 37152–37161.
25 C. Maccato, L. Bigiani, L. Girardi, A. Gasparotto, O. I. Lebedev, E. Modin, D. Barreca and G. A. Rizzi, *Adv. Mater. Interfaces*, 2021, **8**, 2100763.
26 X. Liu, A. Jin, Y. Jia, J. Jiang, N. Hu and X. Chen, *RSC Adv.*, 2015, **5**, 92033–92041.
27 L. Zeng, K. Zhou, L. Yang, G. Du, L. Liu and W. Zhou, *ACS Appl. Energy Mater.*, 2018, **1**, 6279–6287.
28 S. Dresp, F. Dionigi, M. Klingenhof and P. Strasser, *ACS Energy Lett.*, 2019, **4**, 933–942.
29 S. Khatun, H. Hirani and P. Roy, *J. Mater. Chem. A*, 2021, **9**, 74–86.
30 J. Zhang, W. Hu, S. Cao and L. Piao, *Nano Res.*, 2020, **13**, 2313–2322.
31 H. V. Dang, Y. H. Wang and J. C. S. Wu, *Appl. Surf. Sci.*, 2022, **572**, 151346.
32 H. Sun, Y. Shi, W. Shi and F. Guo, *Appl. Surf. Sci.*, 2022, **593**, 153281.
33 S. Dresp, F. Dionigi, S. Loos, J. Ferreira de Araujo, C. Spöri, M. Gliech, H. Dau and P. Strasser, *Adv. Energy Mater.*, 2018, **8**, 1800338.
34 Y. Liu, F.-Y. Su, Y.-X. Yu and W.-D. Zhang, *Int. J. Hydrogen Energy*, 2016, **41**, 7270–7279.
35 W. Xiong, F. Huang and R.-Q. Zhang, *Sustainable Energy Fuels*, 2020, **4**, 485–503.
36 Y. Li, J. Feng, H. Li, X. Wei, R. Wang and A. Zhou, *Int. J. Hydrogen Energy*, 2016, **41**, 4096–4105.
37 Y. Li, R. Wang, H. Li, X. Wei, J. Feng, K. Liu, Y. Dang and A. Zhou, *J. Phys. Chem. C*, 2015, **119**, 20283–20292.
38 H. Xie, Z. Zhao, T. Liu, Y. Wu, C. Lan, W. Jiang, L. Zhu, Y. Wang, D. Yang and Z. Shao, *Nature*, 2022, **612**, 673–678.
39 S. Fukuzumi, Y.-M. Lee and W. Nam, *ChemSusChem*, 2017, **10**, 4264–4276.
40 Y. Kuang, M. J. Kenney, Y. Meng, W.-H. Hung, Y. Liu, J. E. Huang, R. Prasanna, P. Li, Y. Li, L. Wang, M.-C. Lin, M. D. McGehee, X. Sun and H. Dai, *Proc. Natl. Acad. Sci. U.S.A.*, 2019, **116**, 6624–6629.
41 T. Cui, X. Zhai, L. Guo, J.-Q. Chi, Y. Zhang, J. Zhu, X. Sun and L. Wang, *Chin. J. Catal.*, 2022, **43**, 2202–2211.
42 L. Zhang, X. Zhang, C. Wei, F. Wang, H. Wang and Z. Bian, *Chem. Eng. J.*, 2022, **435**, 134873.
43 F. Wang, R. Ou, H. Yu, Y. Lu, J. Qu, S. Zhu, L. Zhang and M. Huo, *Appl. Surf. Sci.*, 2021, **565**, 150597.

44 J. K. George, A. Bhagat, B. Bhaduri and N. Verma, *Catal. Lett.*, 2023, **153**, 419–431.

45 Y. Liu, Y.-X. Yu and W.-D. Zhang, *Int. J. Hydrogen Energy*, 2014, **39**, 9105–9113.

46 K. C. Christoforidis, T. Montini, E. Bontempi, S. Zafeiratos, J. J. D. Jaén and P. Fornasiero, *Appl. Catal., B*, 2016, **187**, 171–180.

47 Z. Jiang, W. Wan, H. Li, S. Yuan, H. Zhao and P. K. Wong, *Adv. Mater.*, 2018, **30**, 1706108.

48 S. Lee and J.-W. Park, *Sustainability*, 2020, **12**, 2866.

49 S. Kang, J. Jang, R. C. Pawar, S.-H. Ahn and C. S. Lee, *RSC Adv.*, 2018, **8**, 33600–33613.

50 N. Wang, L. Wu, J. Li, J. Mo, Q. Peng and X. Li, *Sol. Energy Mater. Sol. Cells*, 2020, **215**, 110624.

51 C. Kim, K. M. Cho, K. Park, K. H. Kim, I. Gereige and H.-T. Jung, *ChemPlusChem*, 2020, **85**, 169–175.

52 J. Wang, X. Zuo, W. Cai, J. Sun, X. Ge and H. Zhao, *Dalton Trans.*, 2018, **47**, 15382–15390.

53 Y. Shen, Q. Han, J. Hu, W. Gao, L. Wang, L. Yang, C. Gao, Q. Shen, C. Wu, X. Wang, X. Zhou, Y. Zhou and Z. Zou, *ACS Appl. Energy Mater.*, 2020, **3**, 6561–6572.

54 Y. Geng, D. Chen, N. Li, Q. Xu, H. Li, J. He and J. Lu, *Appl. Catal., B*, 2021, **280**, 119409.

55 C. Yang, J. Qin, S. Rajendran, X. Zhang and R. Liu, *ChemSusChem*, 2018, **11**, 4077–4085.

56 P. Arora, A. P. Singh, B. R. Mehta and S. Basu, *Vacuum*, 2017, **146**, 570–577.

57 J. Theerthagiri, R. A. Senthil, A. Priya, J. Madhavan, R. J. V. Michael and M. Ashokkumar, *RSC Adv.*, 2014, **4**, 38222–38229.

58 Y. Wu, J. Ward-Bond, D. Li, S. Zhang, J. Shi and Z. Jiang, *ACS Catal.*, 2018, **8**, 5664–5674.

59 R. Khurram, Z. U. Nisa, A. Javed, Z. Wang and M. A. Hussien, *Molecules*, 2022, **27**, 1442.

60 Z. Pan, G. Zhang and X. Wang, *Angew. Chem., Int. Ed.*, 2019, **58**, 7102–7106.

61 Y. Yang, L. Liu, Q. Qi, F. Chen, M. Qiu, F. Gao and J. Chen, *Catal. Commun.*, 2020, **143**, 106047.

62 M. Guo, M. Chen, J. Xu, C. Wang and L. Wang, *Chem. Eng. J.*, 2023, **461**, 142046.

63 Y. Li, X. Wei, X. Yan, J. Cai, A. Zhou, M. Yang and K. Liu, *Phys. Chem. Chem. Phys.*, 2016, **18**, 10255–10261.

64 S. Xiong, X. Liu, X. Zhu, G. Liang, Z. Jiang, B. Cui and J. Bai, *Ecotoxicol. Environ. Saf.*, 2021, **208**, 111519.

65 A. Gasparotto, D. Barreca, D. Bekermann, A. Devi, R. A. Fischer, C. Maccato and E. Tondello, *J. Nanosci. Nanotechnol.*, 2011, **11**, 8206–8213.

66 M. Benedet, G. A. Rizzi, A. Gasparotto, O. I. Lebedev, L. Girardi, C. Maccato and D. Barreca, *Chem. Eng. J.*, 2022, **448**, 137645.

67 Y.-S. Jun, E. Z. Lee, X. Wang, W. H. Hong, G. D. Stucky and A. Thomas, *Adv. Funct. Mater.*, 2013, **23**, 3661–3667.

68 W. Liu, Z. Zhang, D. Zhang, R. Wang, Z. Zhang and S. Qiu, *RSC Adv.*, 2020, **10**, 28848–28855.

69 L. Girardi, G. A. Rizzi, L. Bigiani, D. Barreca, C. Maccato, C. Marega and G. Granozzi, *ACS Appl. Mater. Interfaces*, 2020, **12**, 31448–31458.

70 J. E. Thorne, J.-W. Jang, E. Y. Liu and D. Wang, *Chem. Sci.*, 2016, **7**, 3347–3354.

71 M. E. A. Warwick, K. Kaunisto, D. Barreca, G. Carraro, A. Gasparotto, C. Maccato, E. Bontempi, C. Sada, T.-P. Ruoko, S. Turner and G. Van Tendeloo, *ACS Appl. Mater. Interfaces*, 2015, **7**, 8667–8676.

72 S. Zhang, J. Yan, S. Yang, Y. Xu, X. Cai, X. Li, X. Zhang, F. Peng and Y. Fang, *Chin. J. Catal.*, 2017, **38**, 365–371.

73 http://imagej.nih.gov/ij/, Accessed January, 2023.

74 https://xpspeak.software.informer.com/4.1/, Accessed December, 2022.

75 M. Benedet, G. A. Rizzi, A. Gasparotto, N. Gauquelin, A. Orekhov, J. Verbeeck, C. Maccato and D. Barreca, *Appl. Surf. Sci.*, 2023, **618**, 156652.

76 Z. B. Chen, H. N. Dinh and E. Miller, *Photoelectrochemical Water Splitting: Standards, Experimental Methods, and Protocols*, Springer, 2013.

77 M. Benedet, A. Gasparotto, G. A. Rizzi, D. Barreca and C. Maccato, *Surf. Sci. Spectra*, 2022, **29**, 024001.

78 M. Benedet, G. A. Rizzi, D. Barreca, A. Gasparotto and C. Maccato, *Surf. Sci. Spectra*, 2023, **30**, 014004.

79 S. Benedoue, M. Benedet, A. Gasparotto, N. Gauquelin, A. Orekhov, J. Verbeeck, R. Seraglia, G. Pagot, G. A. Rizzi, V. Balzano, L. Gavioli, V. D. Noto, D. Barreca and C. Maccato, *Nanomaterials*, 2023, **13**, 1035.

80 C. Feng, Z. Wang, Y. Ma, Y. Zhang, L. Wang and Y. Bi, *Appl. Catal., B*, 2017, **205**, 19–23.

81 M. E. A. Warwick, D. Barreca, E. Bontempi, G. Carraro, A. Gasparotto, C. Maccato, K. Kaunisto, T. P. Ruoko, H. Lemmetyinen, C. Sada, Y. Gönüllü and S. Mathur, *Phys. Chem. Chem. Phys.*, 2015, **17**, 12899–12907.

82 H. Tan, J. Verbeeck, A. Abakumov and G. Van Tendeloo, *Ultramicroscopy*, 2012, **116**, 24–33.

83 https://eels.info/atlas.

84 F. Ge, X. Li, M. Wu, H. Ding and X. Li, *RSC Adv.*, 2022, **12**, 8300–8309.

85 F. J. Millero, R. Feistel, D. G. Wright and T. J. McDougall, *Deep Sea Res., Part I*, 2008, **55**, 50–72.

86 X. An, C. Hu, H. Lan, H. Liu and J. Qu, *ACS Appl. Mater. Interfaces*, 2018, **10**, 6424–6432.

87 Y. Surendranath, M. W. Kanan and D. G. Nocera, *J. Am. Chem. Soc.*, 2010, **132**, 16501–16509.

88 M. D. Sharma and M. Basu, *Langmuir*, 2022, **38**, 12981–12990.

89 C. Zachäus, F. F. Abdi, L. M. Peter and R. van de Krol, *Chem. Sci.*, 2017, **8**, 3712–3719.

90 L. M. Peter, K. G. U. Wijayantha and A. A. Tahir, *Faraday Discuss.*, 2012, **155**, 309–322.

91 B. Klahr, S. Gimenez, F. Fabregat-Santiago, T. Hamann and J. Bisquert, *J. Am. Chem. Soc.*, 2012, **134**, 4294–4302.

92 M. Barroso, A. J. Cowan, S. R. Pendlebury, M. Grätzel, D. R. Klug and J. R. Durrant, *J. Am. Chem. Soc.*, 2011, **133**, 14868–14871.

93 D. R. Gamelin, *Nat. Chem.*, 2012, **4**, 965–967.